Title

Reversing neural circuit and behavior deficit in mice exposed to maternal inflammation by Zika virus

Journal

EMBO Reports, 22(8)

ISSN

1469-221X

Authors

Ma, Li
Wang, Jing
Ge, Jianlong
et al.

Publication Date

2021-08-04

DOI

10.15252/embr.202051978

Peer reviewed

Article

TRANSPARENT PROCESS

EMBO reports

Reversing neural circuit and behavior deficit in mice exposed to maternal inflammation by Zika virus

Li Ma[1,†], Jing Wang[2,†], Jianlong Ge[1,3], Yuan Wang[1,4], Wei Zhang[1], Yuanning Du[1], Jun Luo[1,5], Yangping Li[6], Feng Wang[6], Guoping Fan[2], Rong Chen[7], Bing Yao[6], Zhen Zhao[8], Ming-Lei Guo[9], Woong-Ki Kim[10], Yang Chai[1] & Jian-Fu Chen[1,*]

Abstract

Zika virus (ZIKV) infection during pregnancy is linked to various developmental brain disorders. Infants who are asymptomatic at birth might have postnatal neurocognitive complications. However, animal models recapitulating these neurocognitive phenotypes are lacking, and the circuit mechanism underlying behavioral abnormalities is unknown. Here, we show that ZIKV infection during mouse pregnancy induces maternal immune activation (MIA) and leads to autistic-like behaviors including repetitive self-grooming and impaired social memory in offspring. In the medial prefrontal cortex (mPFC), ZIKV-affected offspring mice exhibit excitation and inhibition imbalance and increased cortical activity. This could be explained by dysregulation of inhibitory neurons and synapses, and elevated neural activity input from mPFC-projecting ventral hippocampus (vHIP) neurons. We find structure alterations in the synaptic connections and pattern of vHIP innervation of mPFC neurons, leading to hyperconnectivity of the vHIP-mPFC pathway. Decreasing the activity of mPFC-projecting vHIP neurons with a chemogenetic strategy rescues social memory deficits in ZIKV offspring mice. Our studies reveal a hyperconnectivity of vHIP to mPFC projection driving social memory deficits in mice exposed to maternal inflammation by ZIKV.

Keywords chemogenetics; mouse behaviors; neural circuit; Zika virus
Subject Categories Microbiology, Virology & Host Pathogen Interaction; Molecular Biology of Disease; Neuroscience
DOI 10.15252/embr.202051978 | Received 27 October 2020 | Revised 26 May 2021 | Accepted 31 May 2021 | Published online 7 July 2021

EMBO Reports (2021) 22: e51978

Introduction

Clinical and animal model studies have established that Zika virus (ZIKV) infection during pregnancy leads to congenital Zika syndrome (CZS), which comprises a wide range of abnormalities including microcephaly, intracranial calcification, fetal growth restriction, stillbirth, ocular disorders, craniofacial disproportion, and among others (Brasil *et al*, 2016; Li *et al*, 2016; Ming *et al*, 2016; Shao *et al*, 2016; Honein *et al*, 2017; Martinot *et al*, 2018). Related structural defects in the brain such as microcephaly have been relatively well characterized in cellular and animal models (Li *et al*, 2016; Miner *et al*, 2016; Ming *et al*, 2016; Shao *et al*, 2016). The majority (> 90%) of fetuses from maternal ZIKV exposure have normal brain size and morphology (Shapiro-Mendoza *et al*, 2017; Hoen *et al*, 2018). Despite being asymptomatic at birth, these children have increased risk of developmental delay, abnormal hearing, vision deficiency, impaired neurosensory functions, and cognitive dysfunctions including autism spectrum disorder (ASD; Einspieler *et al*, 2019; Nielsen-Saines *et al*, 2019; Cranston *et al*, 2020; Mulkey *et al*, 2020; Peçanha *et al*, 2020; Soriano-Arandes *et al*, 2020; Wheeler *et al*, 2020). Emerging evidence suggests that infants who are asymptomatic at birth might have higher-order neurocognitive complications that compromise quality of life later on (Adams Waldorf *et al*, 2018). Animal models are required to predict and recapitulate these neurocognitive dysregulations in offspring exposed to maternal ZIKV infection.

1 Center for Craniofacial Molecular Biology, University of Southern California (USC), Los Angeles, CA, USA
2 Department of Human Genetics, David Geffen School of Medicine, University of California Los Angeles, Los Angeles, CA, USA
3 Department of Anesthesiology and Pain Medicine, the University of Texas MD Anderson Cancer Center, Houston, TX, USA
4 State Key Laboratory of Oral Diseases, National Clinical Research Center for Oral Diseases, West China Hospital of Stomatology, Sichuan University, Chengdu, China
5 College of Stomatology, Chongqing Medical University, Chongqing, China
6 Department of Human Genetics, Emory University School of Medicine, Atlanta, GA, USA
7 Department of Diagnostic Radiology and Nuclear Medicine, University of Maryland School of Medicine, Baltimore, MD, USA
8 Zilkha Neurogenetic Institute, Keck School of Medicine, University of Southern California, Los Angeles, CA, USA
9 Department of Pathology and Anatomy, Eastern Virginia Medical School, Norfolk, VA, USA
10 Department of Microbiology and Molecular Cell Biology, Eastern Virginia Medical School, Norfolk, VA, USA
*Corresponding author. Tel: +1 323 442 2062; E-mail: jianfu@usc.edu
†These authors contributed equally to this work

Viral infection during pregnancy is a risk factor for lifelong neuropathology and altered behaviors in offspring (Knuesel *et al*, 2014; Estes & McAllister, 2016). Among these neuropsychiatric abnormalities is ASD, which are characterized by deficits in social interactions and repetitive behaviors. These behavioral abnormalities are often attributed to the dys-connection within and between different brain regions (Geschwind & Levitt, 2007), including the medial prefrontal cortex (mPFC; Amodio & Frith, 2006). Altered excitation and inhibition (E/I) balance in mouse mPFC is sufficient to recapitulate cognitive and emotional behaviors altered in ASD patients (Yizhar *et al*, 2011). Restoring E/I balance in ASD animal models improves social interactions (Selimbeyoglu *et al*, 2017). Overall, E/I imbalance in the cerebral cortex has been proposed to explain behavioral abnormalities in various neuropsychiatric disorders, including ASD and schizophrenia. The mPFC is responsible for integrating various sensory information during higher-order cognitive behaviors (Amodio & Frith, 2006; Euston *et al*, 2012). As an integrator, the mPFC contains a complex network of highly interconnected neurons resulting in a reverberating circuit which is highly sensitive to the changes of its afferent inputs. One of the most potent inputs to the mPFC is from the ventral hippocampus (vHIP). Pyramidal neurons in the vHIP send axonal projections to the mPFC, where they form mono-excitatory glutamatergic synapses with both excitatory and inhibitory neurons in the deep layers of mPFC (Thierry *et al*, 2000; Gabbott *et al*, 2002; Liu & Carter, 2018; Phillips *et al*, 2019). The importance of vHIP-mPFC circuit is broadly appreciated and its disruption is implicated in various neuropsychiatric disorders, including Rett syndrome (Phillips *et al*, 2019), schizophrenia (Sigurdsson *et al*, 2010), anxiety (Padilla-Coreano *et al*, 2016), and depression (Carreno *et al*, 2016). Therefore, cortical function in the mPFC and the neural connectivity between vHIP and mPFC represent reasonable entry points to investigate the circuit defect underlying behavioral abnormalities in offspring exposed to maternal ZIKV infection.

Here, we established a mouse model of maternal ZIKV infection and found that offspring mice exhibited autism-like cognitive behaviors, including impaired social memory and repetitive self-grooming. These behavioral deficits are consistent with disrupted E/I balance leading to cortical hyperactivity, which can be explained by dysregulation of interneurons and inhibitory synapses. Furthermore, our optogenetic studies revealed increased neural connectivity in the vHIP-mPFC pathway, which could further exacerbate the cortical hyperactivity. Importantly, chemogenetic modulation of the activity of mPFC-projecting vHIP neurons, using design receptor exclusively activated by designer drugs (DREADDs), restored social memory deficits in offspring mice exposed to maternal ZIKV infection. Our studies provide a new mouse model of neurocognitive behavioral abnormalities in ZIKV-affected offspring and revealed novel circuit mechanisms underlying these higher-order neurocognitive dysregulations.

Results

ZIKV infection induces maternal immune activation (MIA)

To mimic the natural transmission from mosquitoes to humans, we administered ZIKV (~100 μl of 1.2×10^6 PFU/ml ZIKV virus, Mexican isolate MEX1-44) or vehicle (PBS) as mock by intravenous injection to pregnant female wild-type mice on embryonic day 12.5 (E12.5). At E14.5, there were no obvious morphological changes in the placentas (Fig EV1A–C); ZIKV was not detected in the placentas or embryonic brains (Fig EV1D and E). To determine whether ZIKV infection induces maternal inflammation, we examined cytokine interleukin-17a (IL-17a), a MIA marker (Choi *et al*, 2016). Pregnant mothers infected by ZIKV at E12.5 resulted in a strong induction of serum IL-17a level compared with mock controls at E14.5 (Fig 1A). We also detected mRNA upregulation of the IL-17a receptor subunit A (IL-17Ra) in the fetal brain after maternal ZIKV infection (Fig 1B). MIA leads to an inflammatory response in the developing embryo, which is reflected by the accumulation of choroid plexus (ChP) macrophages (Cui *et al*, 2020). Meninges are sensitive to viral inflammation and meningeal dural sinuses serve as a neuroimmune interface (Kohil *et al*, 2021; Rustenhoven *et al*, 2021). Therefore, we examined macrophages in meninges and choroid plexus of the fetal brain. There was a significantly increased number of macrophages, labeled by Iba1, at meninges in the fetal brain exposed to maternal ZIKV infection (Fig 1E and F). Macrophage activation is reflected by the morphology transition from thin to round shape as well as the expression of CD68, a marker of inflammation associated with macrophages (Fig 1C and D). In ZIKV-affected fetal brains, we detected an increase in the Iba1-positive macrophage numbers in the ChP (Fig 1G and H), in the percentage of macrophages migrated to the ChP surface facing to the cerebrospinal fluid (CSF) (Fig 1G and I), and in the percentages of round-shape macrophages (Fig 1G and J). The CD68-positive macrophages were also significantly increased in the fetal ChP after maternal ZIKV infection (Fig 1K and L). Together, these results suggested that ZIKV infection during pregnancy-induced MIA and the inflammatory response of fetal brains.

Autism-like behaviors in offspring mice exposed to maternal ZIKV infection

We performed behavioral testing, which were not significantly different between male and female offspring mice (Fig EV2D–F); therefore, we focused on combined males and females for the behavioral analysis. In the three-chamber test (Fig 2A), ZIKV-affected offspring mice exhibited normal sociability compared with the mock group. This was reflected by mice from both groups spending more time in the chamber with the stranger mouse (Fig 2B and C) as well as more time sniffing the stranger mouse (Fig 2D), indicating strong preference for the stranger mouse (stranger 1) over an empty wire cup (Fig 2E). In the social memory session, a novel stranger mouse (stranger 2) was placed in the previously empty cup. Mock group mice spent more time interacting with the stranger 2 mouse, as expected. In contrast, ZIKV-affected offspring spent comparable time in these two chambers (Fig 2F and G) and in sniffing (Fig 2H) stranger 1 and stranger 2. There was a significantly decreased discrimination index of stranger 2 versus stranger 1 in ZIKV compared with mock offspring mice (Fig 2I), indicating a social memory deficit. Mice of both groups covered similar distance during the three-chamber test (Fig EV2A), indicating that the reduced interaction with the novel stranger mouse was likely not caused by impaired locomotion. To further validate the social memory deficit, we performed a five-trial social memory test (Fig 2J) to assess social habituation and discrimination abilities. Mice from both groups

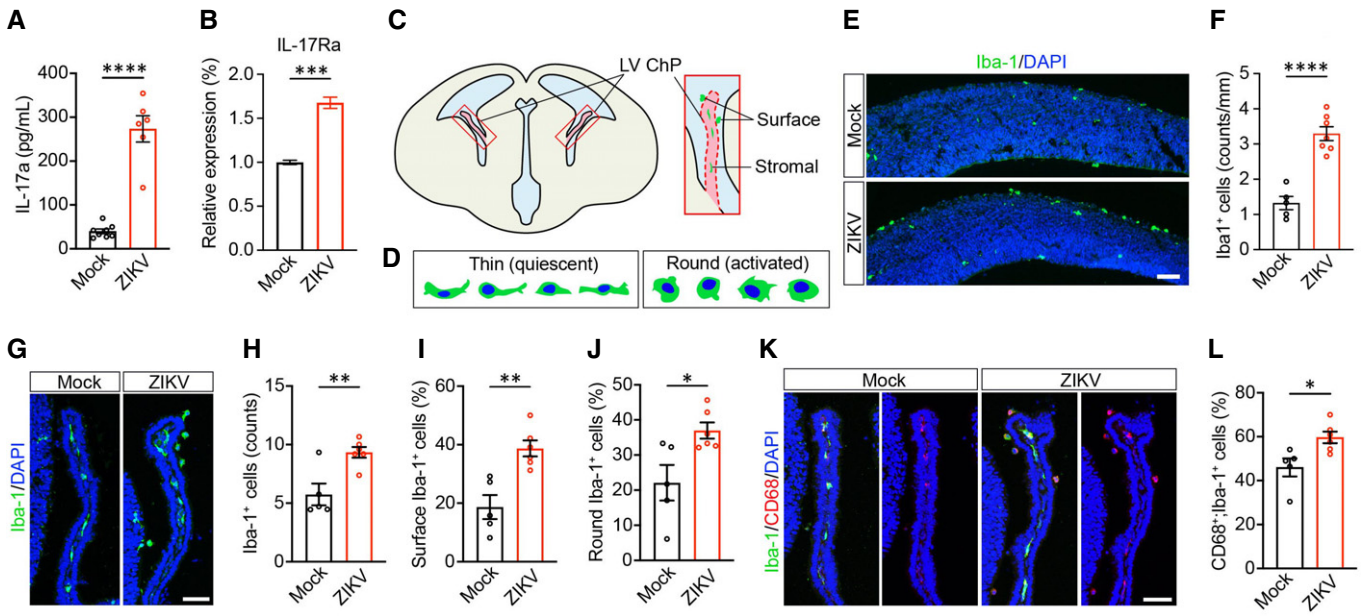

Figure 1. ZIKV infection during pregnancy induces MIA and inflammatory responses in fetal brains.

A ELISA measurement of serum concentrations of maternal IL-17a at E14.5. Mock $n = 8$; ZIKV $n = 6$ mice.
B RT–PCR analysis of IL-17Ra mRNA levels in the embryonic brains at E14.5. Mock $n = 7$; ZIKV $n = 8$ embryos.
C Schematic of the E14.5 brain. LV ChP, lateral ventricular choroid plexus.
D Schematic of morphological states of quiescent and activated Iba1$^+$ macrophages.
E The representative images of IF-IHC staining of E14.5 embryonic brains with antibodies against Iba1 (green) and DAPI (blue). Scale bar, 200 μm.
F Quantification of numbers of Iba1$^+$ cells on the meningeal regions. Mock $n = 5$; ZIKV $n = 7$ embryos.
G The representative images of IF-IHC staining of choroid plexus of E14.5 embryonic brains with antibodies against Iba1 (green) and DAPI (blue). Scale bar, 50 μm.
H Quantification of total number of Iba1$^+$ cells per ChP area.
I Percentage of Iba1$^+$ cells on the surface of ChP.
J Percentage of round-shaped Iba1$^+$ cells.
K The representative images of IF-IHC staining of choroid plexus of E14.5 embryonic brains with antibodies against Iba1 (green), CD68 (red), and DAPI (blue). Scale bar, 50 μm.
L Percentage of CD68$^+$; Iba1$^+$ cells out of total Iba1$^+$ cells.

Data information: *$P < 0.05$, **$P < 0.01$, ***$P < 0.001$, ****$P < 0.0001$, two-tailed unpaired *t*-test. All data are presented as mean ± SEM. Mock $n = 5$; ZIKV $n = 6$ biological replicates in (H–J).

gradually habituated to stranger 1 within the first five trials, before a novel stranger mouse was introduced in the sixth trial. Mock but not ZIKV offspring mice spent dramatically increased interaction time with the novel stranger mouse, which indicated failed discrimination of the novel stimulus in ZIKV offspring mice (Fig 2K and L).

We next performed novel object test. Both groups showed comparable preference for the novel object, suggesting that ZIKV offspring mice had normal novel object recognition ability (Fig EV2B and C). These results suggest that the social memory deficit of ZIKV offspring mice is likely not due to the disruption of novel object recognition. Repetitive behavior is a typical core symptom in ASD patients (Silverman *et al*, 2010; Rothwell *et al*, 2014). Therefore, we performed self-grooming analysis (Fig 2M). ZIKV-affected offspring mice spent significantly more time self-grooming than the mock group (Fig 2N), indicating repetitive behaviors. We did not detect significant differences between male and female mice in these behavioral tests, including three-chamber, five-trial social memory, and self-grooming tests (Fig EV2D–F).

There were no significant differences between ZIKV and control groups in looming spot test (Fig EV3A–H), in the odor discrimination and habituation test (Fig EV3I and J), and in grip strength (Fig EV3K) and rotarod assays (Fig EV3L and M). These negative results suggested that social memory abnormalities in ZIKV-affected offspring mice are likely not due to vision, odor, or locomotion deficits. Interestingly, correlation analyses showed that the social memory deficit in the three-chamber test is positively correlated with performance in the 5-trial social memory test (Fig EV2G) but not with self-grooming behavior (Fig EV2H). These results suggested that the social memory performance of individual mouse affected by ZIKV exposure is relatively consistent in different social behavioral assays and is not predictive for the severity of self-grooming repetitive behavior deficit. We further analyzed the result by dividing the ZIKV-affected offspring into subtle and severe groups based on the severity of social memory deficit (Fig EV2I). However, such difference in three-chamber test is not reflected in the five-trial social memory test as well as in self-grooming test (Fig EV2J and K). Therefore, our models likely could not recapitulate the phenotypical variability in CZS. Taken together, these results suggest that ZIKV-affected offspring mice exhibit autistic-like behaviors including impaired social memory and repetitive self-grooming.

E/I imbalance and increased cortical activity in ZIKV-affected offspring mice

To investigate circuit mechanisms underlying impaired social memory, we focused on the mPFC, which controls social and emotional behaviors altered in ASD (Amodio & Frith, 2006; Forbes & Grafman, 2010). E/I imbalance in wild-type (WT) mouse mPFC is sufficient to cause social behavioral deficits (Yizhar *et al*, 2011), and restoring E/I balance in ASD mouse models improves their social interactions (Selimbeyoglu *et al*, 2017). To investigate E/I balance and synaptic transmission, we performed the whole-cell voltage-clamp recording in layer 5 (L5) pyramidal neurons of mPFC acute slices. In the postnatal day 14 (P14) ZIKV offspring mPFC, pyramidal neurons had higher spontaneous excitatory postsynaptic current (sEPSC) frequency (Fig 3A and B) and lower spontaneous inhibitory postsynaptic current (sIPSC) frequency (Fig 3D and E), suggesting potential changes in synapse numbers or presynaptic vesicle release probability. In contrast, there were no significant differences detected in the amplitude of sEPSC or sIPSC (Fig 3C and F). These results suggested that the balance between cortical excitation and inhibition is shifted to favor excitation over inhibition in ZIKV-affected offspring mice.

Next, we measured the responses of L5 pyramidal neurons to current injection (Fig 3G). A series of depolarizing currents were injected to elicit action potentials, and the resulting firing rates were

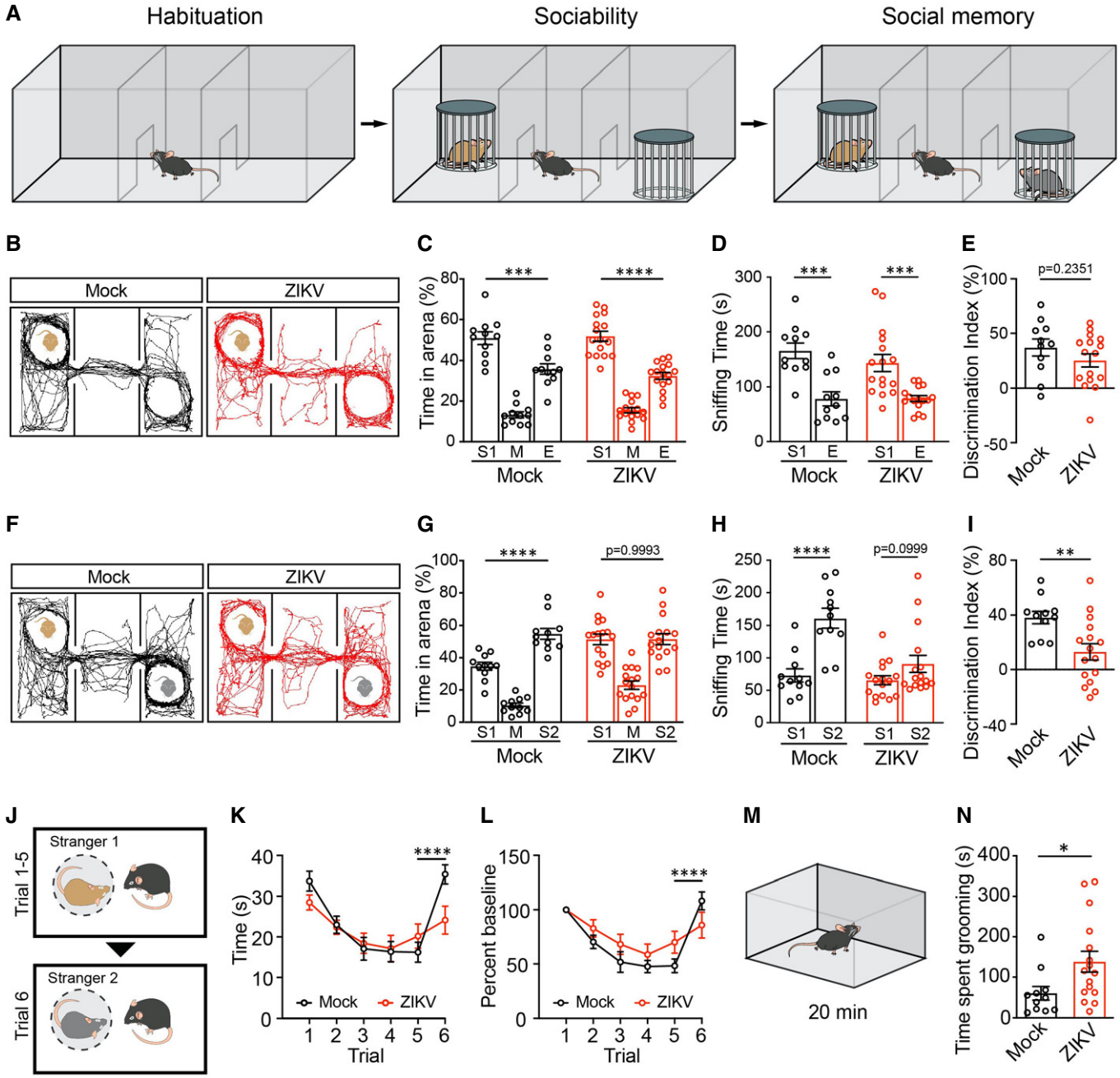

Figure 2.

Figure 2. Autism-like behaviors in ZIKV-affected offspring mice.

A Schematic of three-chamber test.
B Representative animal tracks in the sociability test.
C Percentage of time the subject mice spent in each chamber in the sociability session of three-chamber test. Mock (n = 11) stranger 1 (S1) chamber vs. empty (E) chamber; ZIKV (n = 16) stranger 1 chamber vs. empty chamber; one-way ANOVA with Bonferroni *post hoc* test.
D Quantification of time spent investigating the stranger mouse and empty cage during sociability session. Mock (n = 11) sniffing time at stranger 1 mouse vs. empty cup, ZIKV (n = 16) sniffing time at stranger 1 mouse vs. empty cup.
E Preference indices in sociability. Mock (n = 11) vs. ZIKV (n = 16).
F Representative animal tracks in the social memory test.
G Percentage of time the subject mice spent in each in the social memory session. Mock (n = 11) stranger 1 (S1) chamber vs. stranger 2 (S2) chamber, $P < 0.0001$; ZIKV (n = 16) stranger 1 chamber vs. stranger 2 chamber; one-way ANOVA with Bonferroni *post hoc* test.
H Quantification of time spent investigating the familiar mouse and novel stranger mouse during social memory session. Mock (n = 11) sniffing time at stranger 1 vs. stranger 2 mouse; ZIKV (n = 16) sniffing time at stranger 1 vs. stranger 2 mouse.
I Preference indices in the social memory session of the three-chamber test. Mock (n = 11) vs. ZIKV (n = 16).
J Schematics of five-trial social memory test.
K Sniffing time in each trial of the five-trial social memory test. Mock (n = 11) trial 5 vs. trial 6; ZIKV (n = 16) trial 5 vs. trial 6.
L Normalized sniffing time in each trial of the five-trial social memory test. Mock (n = 11) trial 5 vs. trial 6; ZIKV (n = 16) trial 5 vs. trial 6.
M Schematics of the self-grooming test.
N Time spent grooming in the self-grooming test. Mock (n = 11) vs. ZIKV (n = 16).

Data information: All data were presented as mean ± SEM. *$P < 0.05$, **$P < 0.01$, ***$P < 0.001$, ****$P < 0.0001$, two-tailed unpaired t-test unless described otherwise; n represent biological replicates.

plotted as a function of increasing current amplitude (F–I curves). The F–I curve analysis showed that L5 pyramidal neurons from ZIKV offspring mice exhibited hyperexcitability (Fig 3H). L5 pyramidal neurons can be divided into two subpopulations based on their projections either subcortically to the pons [corticopontine (CPn)] or to the contralateral cortex [commissural (COM)] (Fig 3I and K; Dembrow *et al*, 2010). Further analyses showed that the changes in neuronal excitabilities of L5 pyramidal neurons were not subpopulation-specific, since both CPn and COM neurons in ZIKV offspring mice exhibited increased action potential frequencies when given over 400 pA current injections (Fig 3J and L). To determine the causes of this hyperexcitability, we examined a series of intrinsic properties of the recorded neurons. The resting membrane potential was not significantly changed between the two groups (Fig EV4A); the action potential (AP) threshold for triggering the first spike during the depolarizing step was similar under the two conditions (Fig EV4B); and the input resistance (R_{in}) in each cell throughout the duration of the recording was not significantly different between mock and ZIKV offspring mice (Fig EV4C). In addition, ZIKV and mock groups exhibited no significant differences in AP amplitude (Fig EV4D), AP duration (Fig EV4E), afterhyperpolarization (AHP) amplitude (Fig EV4F), or frequency accommodation (Fig EV4G). These results suggest that intrinsic electrophysiological properties of mPFC pyramidal neurons are normal in ZIKV offspring mice.

To confirm the increased cortical activity in ZIKV-affected offspring mice, we used c-Fos to monitor neural activity. The subject mice were co-housed with their littermates for 2 weeks, then allowed to interact with a novel stranger mouse or a co-housed littermate as a baseline for 20 min. Two hours after social exposure, brain samples were collected for immunofluorescence (IF) staining using antibodies against c-Fos (Fig EV5A and D). The c-Fos-positive neurons were significantly increased in the prelimbic (PL) mPFC regions in ZIKV-affected offspring mice compared with mock controls in both experimental paradigms (Fig EV5B, C, E, and F), whereas they were increased in infralimbic (IL) mPFC regions of ZIKV offspring mice in response to the co-housed littermate but not the novel stranger mouse (Fig EV5C and F). Together, these results revealed an E/I imbalance and cortical hyperactivity in ZIKV-affected offspring mice.

Dysregulation of inhibitory neurons and synapses in ZIKV-affected offspring mice

To investigate the neural substrate of increased circuit excitability, we determined whether pyramidal neuron hyperexcitability in the mPFC is caused by the dysregulation of local inhibitory neurons or synaptic changes in the mPFC of ZIKV-affected offspring. We performed IF staining using antibodies against three main interneuron markers, parvalbumin (PV), somatostatin (SST), and calretinin (CAL) (Kepecs & Fishell, 2014). There was a significantly decreased number of PV^+ neurons in both PL and IL cortices of the ZIKV group compared with mock control (Fig 4A and B). CAL^+ neurons were decreased in the PL but not IL cortex (Fig 4A and F), while SST^+ neurons were similar in both PL and IL cortices in ZIKV-affected offspring mice compared with mock controls (Fig 4A and D). In addition, the numbers of PV^+ neurons in both PL and IL cortices were positively correlated with social preference for the novel stranger mouse in the social memory session of the three-chamber test (Fig 4C), whereas SST^+ and CAL^+ neurons were not correlated with the social preference result (Fig 4E and G). Consistent with this interneuron dysregulation, the density of inhibitory vesicular GABA transporter (vGAT) puncta was reduced in the mPFC of ZIKV-affected offspring mice (Fig 4J and K). In contrast, we did not find significant changes in the number of excitatory synaptic puncta positive for the vesicular glutamate transporter 1 (vGLUT1) (Fig 4H and I). Together, these results suggest that the dysregulation of inhibitory neurons and synapses might contribute to the pyramidal neuron hyperexcitability in the mPFC of ZIKV-affected offspring mice.

Hyperconnectivity of vHIP to mPFC projections in ZIKV-affected offspring mice

In addition to the inhibitory synaptic drive dysregulation described above, the increased cortical activity in the mPFC of ZIKV offspring

mice could be due to increased excitatory inputs. As one of the most potent inputs to the mPFC, pyramidal neurons in the vHIP send axonal projections to form mono-excitatory glutamatergic synapses with neurons in the deep layers of mPFC (Thierry *et al*, 2000; Gabbott *et al*, 2002; Phillips *et al*, 2019). We also observed the significantly increased number of c-Fos^{+} neurons in the vHIP of ZIKV-affected offspring (Fig EV5G). Therefore, we hypothesized that the vHIP-mPFC circuit is altered in ZIKV-affected offspring mice, contributing to their social memory deficit. To test this hypothesis, we examined neural activity in mPFC-projecting vHIP neurons. To mark them, we injected an AAV vector carrying the reporter mCherry (AAV-DIO-mCherry), expressed in a Cre-dependent manner, into vHIP CA1 regions. Meanwhile, a retrograde-transporting AAVretro-Cre virus was injected into the

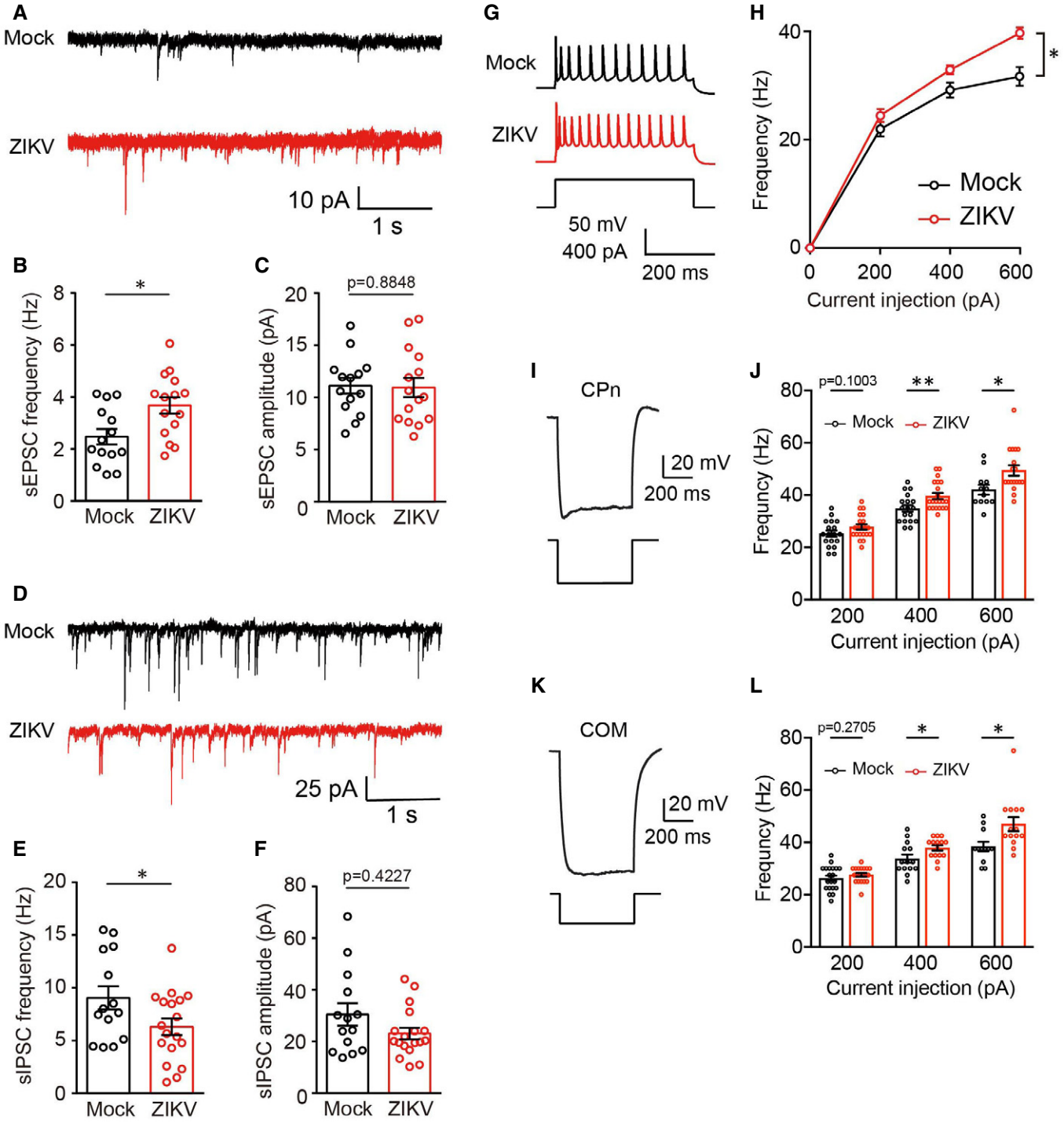

Figure 3.

Figure 3. Increased excitatory and inhibition (E–I) ratio and excitability in ZIKV-affected offspring brains.

A Representative recordings of sEPSCs from pyramidal neurons in mPFC.
B Quantitation of sEPSC frequency mPFC from pyramidal neurons in mPFC.
C Quantitation of sEPSC amplitude of mPFC pyramidal neurons. Mock, $n = 14$ neurons from 4 mice; ZIKV, $n = 15$ neurons from 5 mice in B and C.
D Representative recordings of sIPSCs from pyramidal neurons in mPFC.
E Quantifications of sIPSC frequency from pyramidal neurons in mPFC.
F Quantifications of sIPSC amplitude of mPFC pyramidal neurons. Mock, $n = 14$ neurons from 5 mice; ZIKV, $n = 18$ neurons from 6 mice in E and F.
G Sample traces evoked by a depolarizing current stimulation of 400 pA.
H Frequency-current (F–I) plots. mock ($n = 20$ neurons, 5 mice) vs. ZIKV ($n = 22$ neurons, 6 mice), $P = 0.0140$.
I Representative traces from CPn neurons in response to a hyperpolarizing current.
J Action potential frequencies of CPn neurons evoked by accelerating current injection. 200 pA: mock $n = 18$; ZIKV $n = 21$ neurons, $P = 0.1003$; 400 pA: mock $n = 18$; ZIKV $n = 21$ neurons, $P = 0.0085$; 600 pA: mock $n = 12$; ZIKV $n = 18$ neurons, $P = 0.0169$.
K Representative traces from COM neurons in response to a hyperpolarizing current.
L Action potential frequencies of COM neurons evoked by accelerating current injection. 200 pA: mock $n = 20$; ZIKV $n = 20$ neurons, $P = 0.2705$; 400 pA: mock $n = 15$; ZIKV $n = 15$ neurons, $P = 0.0345$; 600 pA: mock $n = 12$; ZIKV $n = 14$ neurons, $P = 0.0160$. Mock $n = 7$; ZIKV $n = 8$ mice in J and L.

Data information: Data were collected from PL and IL regions of mPFC, and were presented as mean ± SEM. $^*P < 0.05$, $^{**}P < 0.01$. Two-tailed unpaired *t*-test unless described otherwise.

mPFC (Fig 5A). After 4–6 weeks, we performed IF staining with antibodies against c-Fos (Fig 5B). The percentage of c-Fos$^+$; mCherry$^+$ double-positive cells out of the total mCherry$^+$ cells was significantly increased in the ZIKV offspring mice compared with mock controls (Fig 5B and C), indicating that mPFC-projecting vHIP neurons were aberrantly activated in ZIKV offspring mice. To determine how the activation of mPFC-projecting vHIP neurons functionally affects mPFC activity, we examined the vHIP-mPFC connectivity strength using optogenetic approaches (Fig 5D). AAV-hChR2-mCherry was injected into vHIP CA1 regions, and after three weeks to allow its anterograde transfer and expression, we confirmed mPFC-projecting presynaptic terminals from vHIP as visualized by mCherry expression (Fig 5E). We applied a blue light (365 nm) to evoke excitatory postsynaptic currents (EPSCs) in the mPFC. The amplitude of evoked EPSCs of pyramidal neurons was significantly larger in the ZIKV group than in the mock controls (Fig 5F and G). Together, these results revealed a hyperactive vHIP-mPFC connection in ZIKV-affected offspring mice.

To investigate the structural basis underlying this hyperactive vHIP-mPFC pathway, we examined the synaptic connection and vHIP innervation pattern of mPFC neurons. We sparsely visualized the vHIP afferent axon terminals in the mPFC by highly diluted AAV-eGFP injection into the vHIP and analyzed the number and size of the synaptic boutons in the mPFC (Fig 6A and B). There was a significant increase in the bouton density in ZIKV-affected offspring mice compared with mock controls, whereas no obvious difference in bouton size was observed between the two groups (Fig 6C and D). Next, we examined the distribution patterns of mPFC neuronal types innervated by vHIP neurons. AAV1-Cre as an anterograde tracer was injected into vHIP regions of Ai14 mice to mark the mPFC neurons post-synaptically innervated by vHIP afferents (Fig 6E). Subtypes of postsynaptic neurons were characterized by co-labeling with different neuronal type markers, including CaMKIIa$^+$ excitatory neurons, PV$^+$, SST$^+$, and CAL$^+$ inhibitory neurons. There was a significant decrease in the PV$^+$ neurons innervated by vHIP afferents in ZIKV-affected offspring mice compared with mock controls (Fig 6F–H). To determine whether reduced PV neuron innervation was due to decreased mPFC-projecting vHIP neurons, we examined vHIP afferent numbers. The retrograde dye CTB was injected into the mPFC of vGLUT1-Cre::Ai14 mice (Fig 6I), in which all the vGLUT1$^+$ excitatory neurons were labeled with tdTomato. The percentages of CTB$^+$; tdTomato$^+$ neurons were comparable in the vHIP regions between ZIKV and mock groups (Fig 6J and K). These results showed that approximately 90% of mPFC-projecting vHIP cells were excitatory neurons, and their numbers were similar between the two groups. Together, these results revealed increased synaptic bouton densities and decreased PV$^+$ neuron innervations in the mPFC, which could serve as the neural structural substrate responsible for the hyperactive vHIP-mPFC pathway in ZIKV-affected offspring mice.

Social memory deficits were rescued by inhibition of the activity of mPFC-projecting vHIP neurons

We hypothesized that the hyperactive vHIP-mPFC circuit drives social memory deficits in ZIKV-affected offspring mice. To test this hypothesis and determine the functional significance of this circuit's hyperactivity, we used a virus-based chemogenetic approach known as designer-receptor-exclusively-activated-by-designer-drugs (DREADD; Sternson & Roth, 2014) to selectively reduce the activity of mPFC-projecting vHIP neurons followed by social memory behavioral studies. We injected AAVretro-Cre into the mPFC (AP + 1.7 mm, ML ± 0.3 mm, DV −1.8 mm). After 2–7 days, a second injection of AAV2-hSyn-DIO-hM4Di-mCherry or AAV2-hSyn-DIO-mCherry (negative control) was applied into the vHIP (AP −3.3 mm, ML ± 3.5 mm, DV −3 mm) (Fig 7A). IF staining confirmed the successful labeling of mPFC-projecting vHIP neurons (Fig 7B). About 4–6 weeks after the second injection, clozapine n-oxide (CNO) was injected to inhibit the activity of mPFC-projecting vHIP neurons one hour before behavioral tests. The social memory deficit was reversed in the CNO-treated hM4Di-expressing ZIKV offspring mice, whereas it was not restored in ZIKV offspring mice expressing mCherry alone (Fig 7C and D). Meanwhile, the inhibition of mPFC-projecting vHIP neuronal activity failed to rescue the increased self-grooming behavior (Fig EV5H) and did not affect the locomotion of ZIKV offspring mice (Fig EV5I). To confirm the inhibition of mPFC-projecting vHIP neuronal activity in CNO-treated hM4Di mice, we measured the percentage of c-Fos$^+$ mPFC-projecting vHIP neurons two hours after the three-chamber test. The percentage of c-Fos$^+$ mPFC-projecting vHIP neurons was significantly reduced in CNO-injected

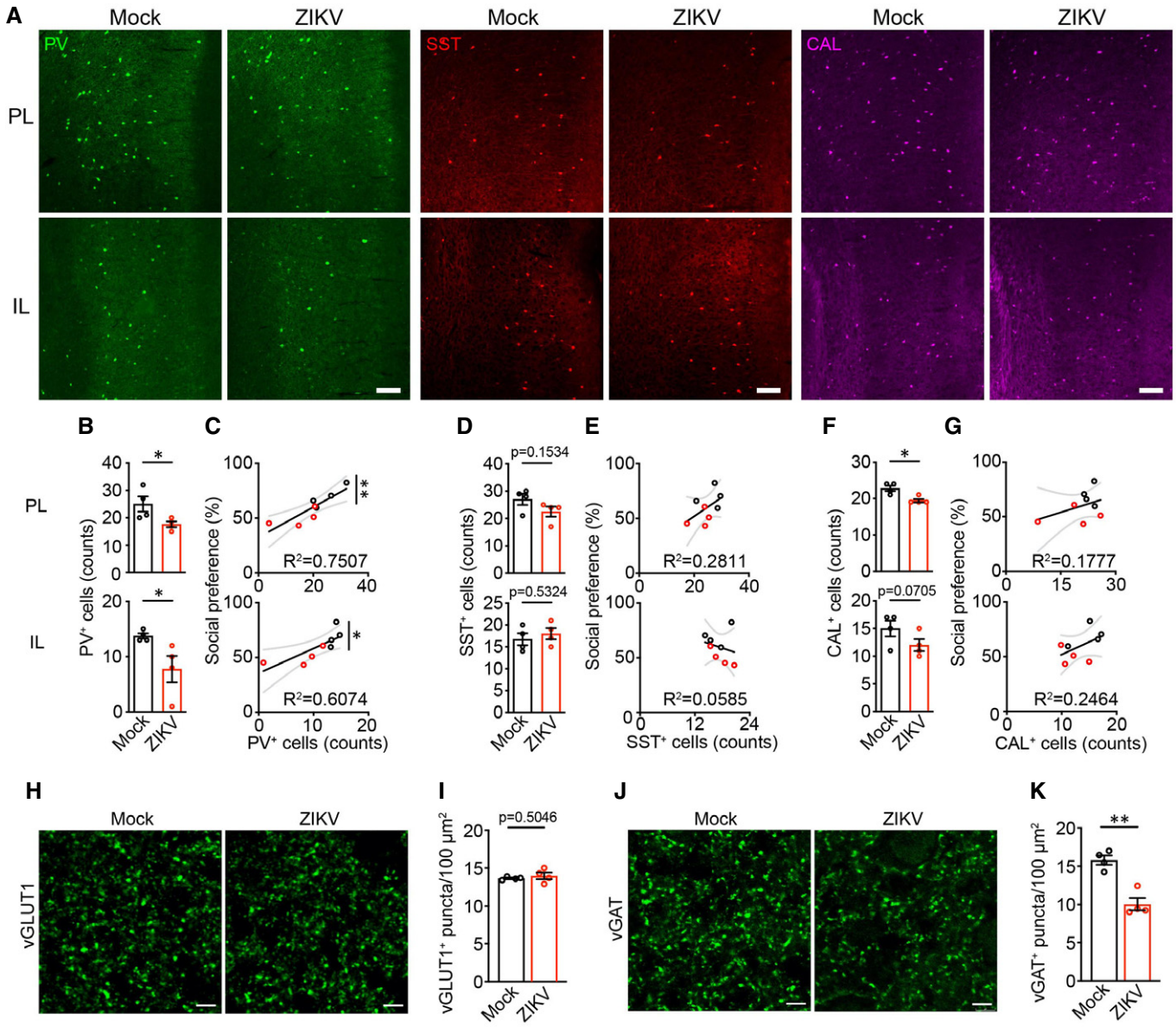

Figure 4. Dysregulation of inhibitory neurons and synapses in ZIKV-affected offspring mice.

A Representative images of PV^+, SST^+, and CAL^+ cells in the prelimbic (PL, upper panel) and infralimbic (IL, lower panel) cortex. Scale bars: 200 μm.

B Quantification of PV^+ cells in the PL and IL cortex.

C PV^+ interneuron numbers plotted against social preference.

D Quantification of SST^+ cells in the PL and IL cortex.

E SST^+ interneuron numbers plotted against social preference.

F Quantification of CAL^+ cells in the PL and IL cortex. Mock, $n = 4$ mice; ZIKV, $n = 4$ mice in B, D, and F. $P = 0.0490$ (PL in B), 0.0253 (IL in B), 0.0113 (PL in F).

G CAL^+ interneuron numbers plotted against social preference. Black solid lines represent regression line; gray lines indicate 95% confidence intervals in C, E, and G. Mock (black circles), $n = 4$ mice; ZIKV (red circles), $n = 4$ mice. $P = 0.0054$ (PL in C), 0.0226 (IL in C), 0.1765 (PL in E), 0.5840 (IL in E), 0.2983 (PL in G), 0.2109 (IL in G); linear regression.

H IF staining of mPFC stained with antibodies against vGLUT1. Scale bars, 5 μm.

I Quantification of $vGLUT1^+$ puncta numbers out of 100 μm^2 region. Mock, $n = 4$ mice; ZIKV, $n = 4$ mice.

J IF staining of mPFC stained with antibodies against vGAT. Scale bars, 5 μm.

K Quantification of $vGAT^+$ puncta numbers out of 100 μm^2 region. Mock, $n = 4$ mice; ZIKV, $n = 4$ mice.

Data information: All data are presented as mean ± SEM. $^*P < 0.05$, $^{**}P < 0.01$. Two-tailed unpaired *t*-test unless described otherwise.

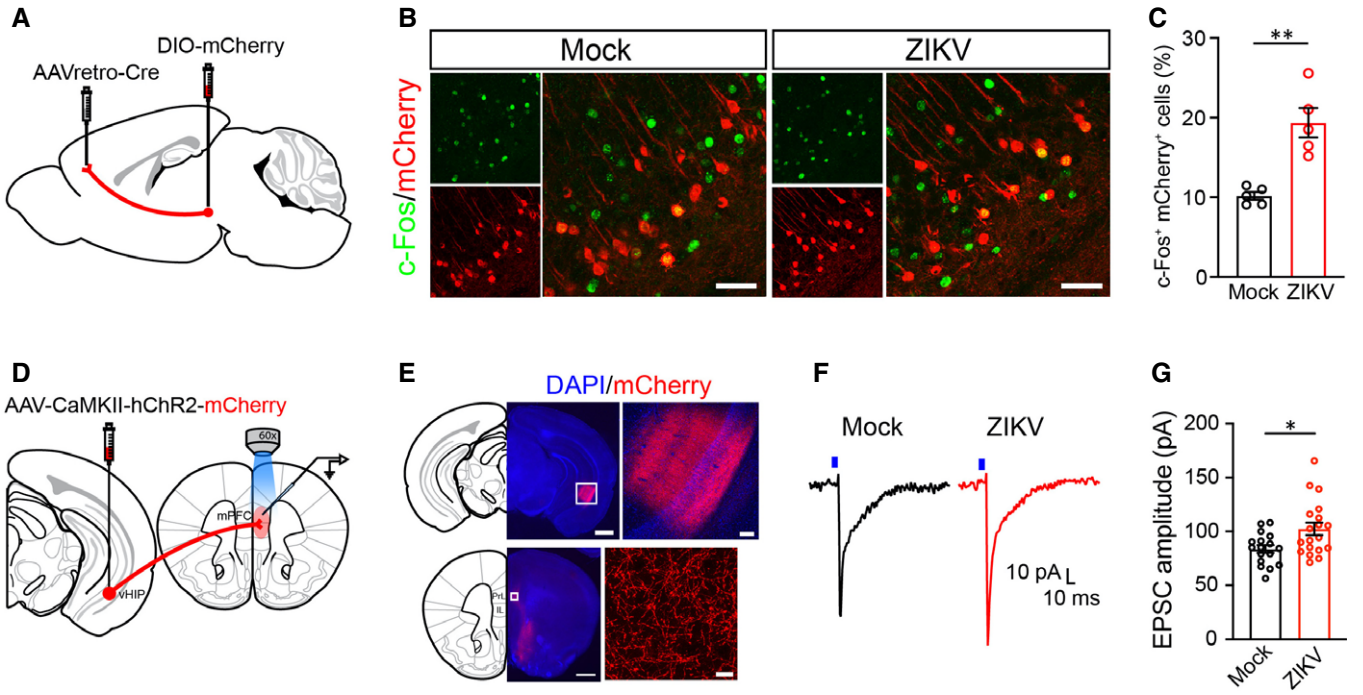

Figure 5. Hyperconnectivity of vHIP-mPFC circuit in mice exposed to maternal ZIKV infection.

A Schematic of mPFC-projecting ventral hippocampus (vHIP) neurons. AAVretro-Cre represents a retrograde-transporting AAV virus expressing Cre; DIO-mCherry is a Cre-dependent mCherry reporter.

B Representative confocal images of the vHIP stained with mCherry (red) and c-Fos (green).

C Quantification of mCherry and c-Fos double-positive cells out of total mCherry-positive cells in the vHIP CA1 regions. Scale bar, 50 μm. Mock (n = 5 mice) vs. ZIKV (n = 5 mice), P = 0.0013.

D Slice recording paradigm. AAV-CaMKII-hChR2-mCherry was injected into vHIP CA1 region and LED (365 nm) was applied to the mPFC.

E Top, mCherry expression at the injection site. Bottom, mCherry-labeled axons in the mPFC. Scale bars, 200 μm and 10 μm in the zoomed areas.

F Representative EPSC traces of the pyramidal neurons in the mPFC. Blue boxes indicate the 470 nm light stimulation.

G Quantification of EPSC amplitude of the pyramidal neurons in the mPFC (PL and IL). Mock (n = 17 neurons from 5 mice) vs. ZIKV (n = 19 neurons from 5 mice), P = 0.0122.

Data information: Data were presented as mean ± SEM. *P < 0.05, **P < 0.01, Two-tailed unpaired t-test unless described otherwise.

mCherry-expressing ZIKV offspring compared with the control group (Fig 7E and F). Together, these results suggested that hyperactivity of the vHIP-mPFC circuit causes social memory deficits in ZIKV-affected offspring mice.

Discussion

We developed a new mouse model of neurocognitive behavioral abnormalities in offspring exposed to maternal ZIKV infection, which induced MIA and inflammatory responses in fetal brains. Our neuropathological studies revealed an impaired E/I balance and cortical hyperactivity coupled with interneuron dysregulation. We identified hyperconnectivity of vHIP to mPFC projections that drive the social memory deficits in ZIKV-affected offspring mice.

Impaired social memory and increased self-grooming in ZIKV-affected offspring mice represent social interaction deficits and repetitive behaviors, which are frequently seen in ASD patients (Silverman *et al*, 2010; Sahin & Sur, 2015; de la Torre-Ubieta *et al*, 2016). Although infants with maternal ZIKV exposure are likely too young to be conclusively assessed neuropsychiatric disorders, available evidences suggest that those children are at increased risk of higher-order cognitive and motor dysfunctions that might compromise the quality of their life later on (Einspieler *et al*, 2019; Nielsen-Saines *et al*, 2019; Cranston *et al*, 2020; Mulkey *et al*, 2020; Peçanha *et al*, 2020; Soriano-Arandes *et al*, 2020; Wheeler *et al*, 2020). Emerging consensus is that long-term monitoring and intervention need to be implemented to identify and address higher-order neurocognitive deficits in children with congenital ZIKV infection or exposure (Adams Waldorf *et al*, 2018; Pessoa *et al*, 2018). Therefore, our animal model has prognostic value and provides a foundation for downstream mechanistic and therapeutic studies. In addition to animal models of ZIKV-associated microcephaly (Ming *et al*, 2016), various animal models have been generated to model postnatal brain defects associated with ZIKV infection. It has been reported that intrauterine ZIKV infection results in paralysis in adulthood in mice (Cui *et al*, 2017; Shi *et al*, 2018); congenital ZIKV infection leads to visual and motor deficits in adult mice (Cui *et al*, 2017); and prenatal ZIKV infection in immunocompetent mice causes postnatal growth deficits and spatial learning deficits(Paul *et al*, 2018; Stanelle-Bertram *et al*, 2018). All these studies introduced the ZIKV pathogen directly into the developing mouse brains.

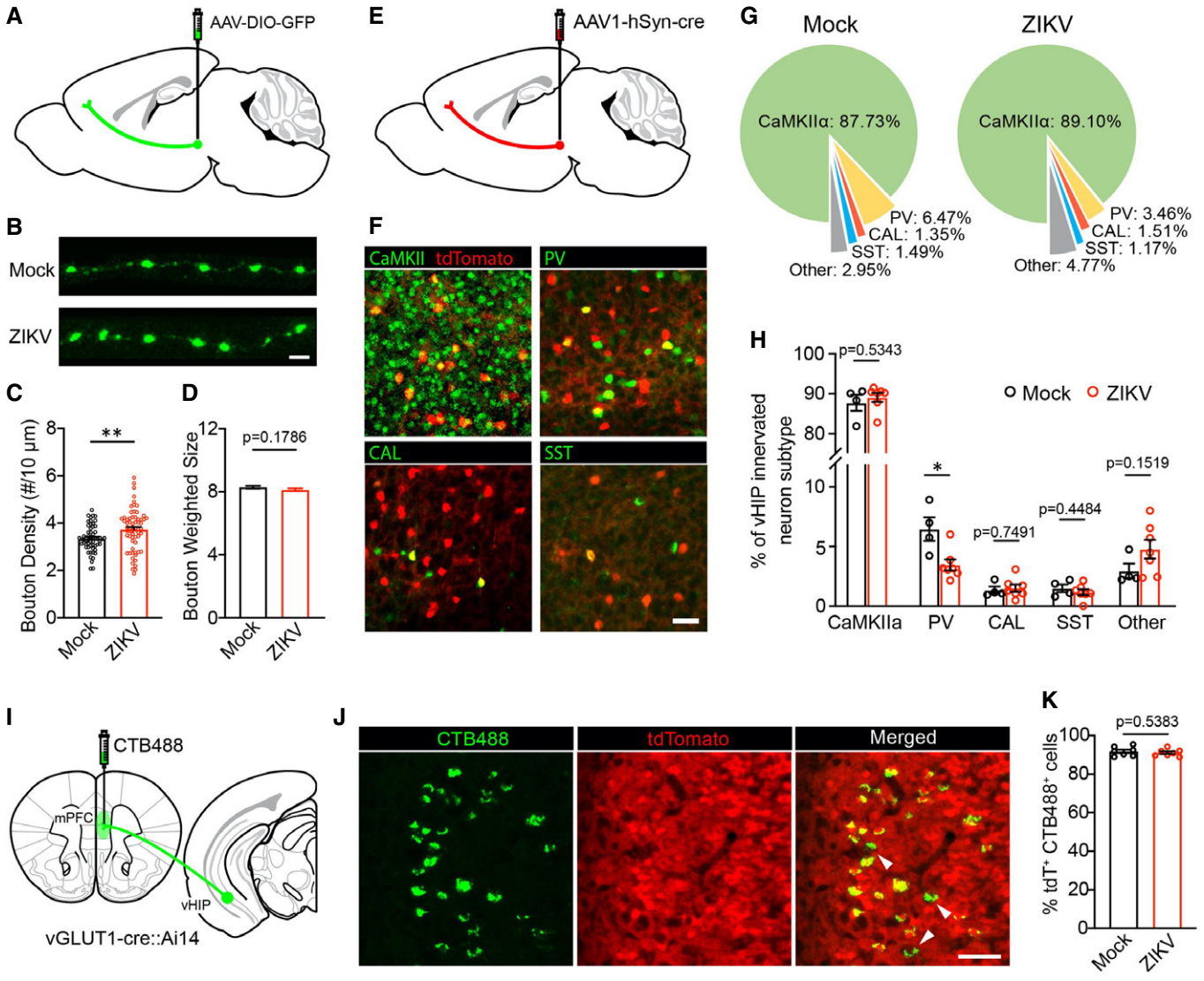

Figure 6. Synaptic connection and pattern of vHIP innervation of mPFC neurons.

A Schematic tracing of presynaptic boutons from vHIP neurons using AAV-DIO-GFP virus.

B Representative examples of GFP-labeled presynaptic boutons. Scale bars: 2.5 μm.

C Quantification of presynaptic bouton density and weighted size in the mPFC (PL and IL). Mock: n = 57 axons from 6 mice; ZIKV: n = 63 axons from 7 mice.

D Quantification of presynaptic bouton weighted size in the mPFC (PL and IL). Mock: n = 2974 boutons from 6 mice; ZIKV: n = 3486 boutons from 7 mice.

E Trans-synaptic tracing of vHIP-derived neurons in the mPFC. AAV1-hSyn-Cre injection in the ventral hippocampus (vHIP) of Ai14 mouse followed by examination of neuronal types in the mPFC.

F Representative confocal images of co-labeled tdTomato and neuronal markers including CaMKII, PV, CAL, and SST in the mPFC. Scale bar, 50 μm.

G Quantification of the percentages of mPFC neuron subtypes innervated by vHIP afferent axons.

H Comparisons of percentages of vHIP-innervated mPFC (PL and IL) neuron subtypes. Mock, n = 4 mice; ZIKV, n = 7 mice. P = 0.5343 in CaMKIIa, 0.0117 in PV, 0.7491 in CAL, 0.4484 in SST, 0.1519 in other uncharacterized neuron subtypes.

I Schematic tracing of a retrograde dye CTB488-labeled vHIP neurons projecting toward mPFC. CTB488 was injected into the mPFC of vGLUT1-Cre::Ai14 mice followed by IF staining in vHIP.

J Representative confocal images of CTB488-labeled tdTomato-positive neurons in the vHIP. White arrowheads indicate CTB488 single positive neurons. Scale bars: 200 μm.

K Quantification of the percentage of tdTomato;CTB488 double-positive cells out of total CTB488-positive cells. Mock, n = 7 mice; ZIKV, n = 7 mice.

Data information: All data were presented as mean ± SEM. *P < 0.05, **P < 0.01, Two-tailed unpaired t-test unless described otherwise.

Our studies differ from those previous reports since our mouse model better mimics maternal–fetal transmission and recapitulates neurocognitive dysregulation without actual ZIKV infection in the offspring mice. Our results further suggest that these behavioral abnormalities are likely caused by MIA, which is consistent with poly-functional immune activation detection in amniotic fluid from

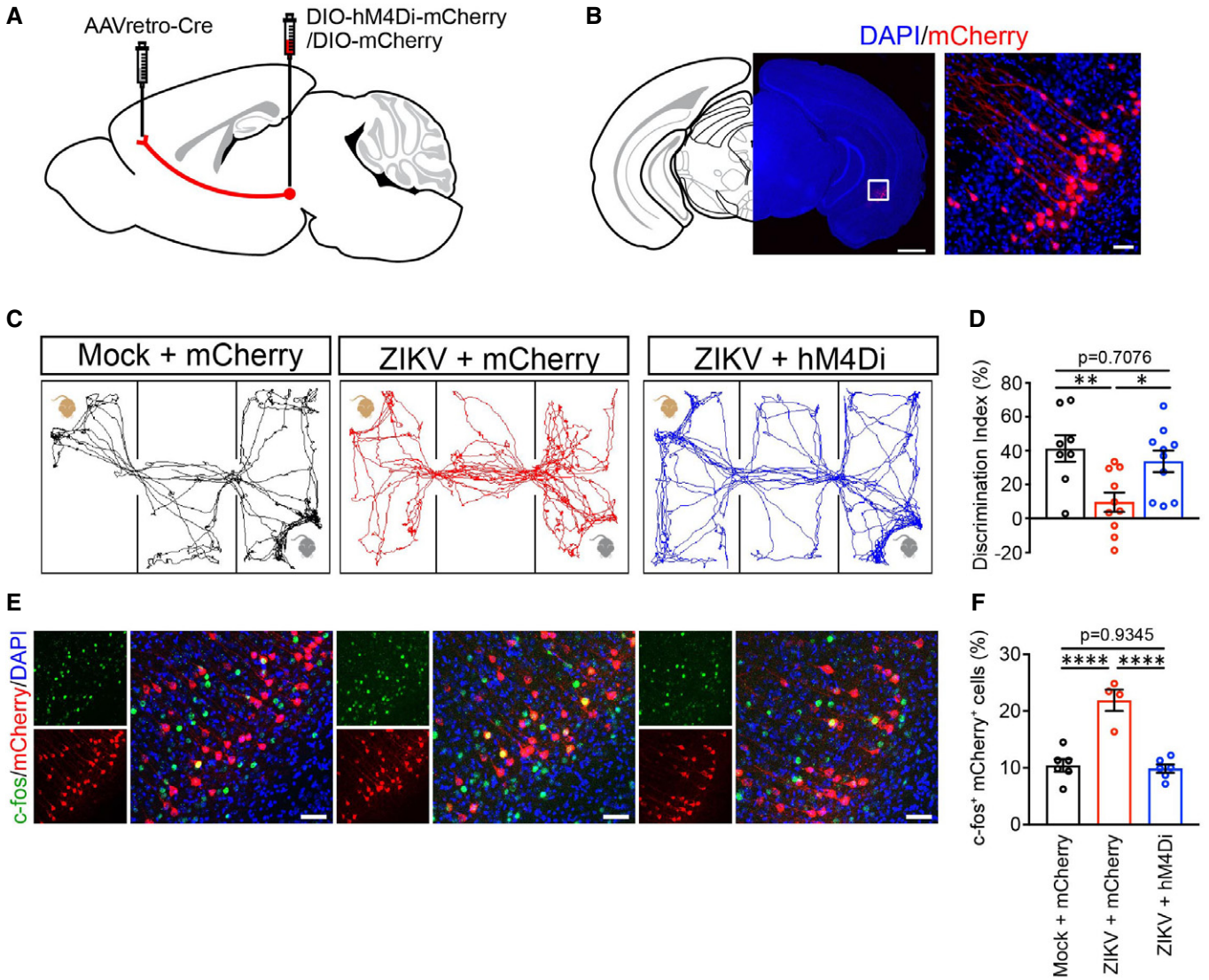

Figure 7. Reducing vHIP-mPFC circuit activity rescued social memory deficit in ZIKV-affected offspring mice.

A Schematic of AAVretro-Cre and AAV-DIO-hM4Di-mCherry or AAV-DIO-mCherry injections.

B mCherry-labeled axons in the vHIP. Scale bars, 200 μm (left panel), and 50 μm (right panel).

C Representative animal tracks in three-chamber test.

D Discrimination indices of the social memory session of three-chamber test. mCherry mock, $n = 8$ mice; mCherry ZIKV, $n = 10$ mice; hM4Di ZIKV $n = 10$ mice, mCherry mock vs. mCherry ZIKV $P = 0.0041$; mCherry ZIKV vs. hM4Di ZIKV $P = 0.0115$; and mCherry mock vs. hM4Di ZIKV $P = 0.7076$.

E Representative confocal images of mCherry (red) and c-Fos (green) double-labeled cells in the vHIP CA1 regions. Scale bars, 50 μm.

F Quantification of the percentage of c-fos; mCherry double-positive cells out of total mCherry cells. mCherry mock, $n = 6$ mice; mCherry ZIKV, $n = 4$ mice; hM4Di ZIKV $n = 6$ mice.

Data information: All data are presented as mean ± SEM. *$P < 0.05$, **$P < 0.01$, ****$P < 0.0001$, one-way ANOVA with Tukey *post hoc* test.

ZIKV-infected patients (Ornelas *et al*, 2017). Future studies should compare our ZIKV model with other MIA animal models to study the common pathogenesis underlying maternal infection-associated risks of neuropsychiatric disorders.

Our electrophysiological analysis revealed E/I imbalance and cortical hyperactivity as the neural substrate underlying behavioral abnormalities in ZIKV-affected offspring mice. The balance between excitatory synapses and inhibitory synapses is a key factor controlling neural circuit functions and can be disrupted by various genetic and environmental risk factors associated with ASD (Yizhar *et al*, 2011; Bateup *et al*, 2013; Selimbeyoglu *et al*, 2017). However, the E/I imbalance in ASD needs to be interpreted in specific brain regions, cell types, and synaptic connections relevant to defined behavioral outcomes (Rothwell *et al*, 2014; Golden *et al*, 2018; Sohal & Rubenstein, 2019). ZIKV-affected offspring mice exhibited decreased expression of parvalbumin (PV) and calretinin (CAL), which label different subtypes of interneurons (Kepecs & Fishell, 2014). Inhibitory synapses labeled by vGAT were correspondingly reduced. This

reduction in PV and CAL immunoreactivity in ZIKV-affected offspring mice is consistent with poly(I:C) MIA mouse models (Shin Yim *et al*, 2017) and could reflect a reduction in interneuron numbers or their expression. Loss of PV^+ neurons and/or decreased PV expression have been documented in ASD patients (Zikopoulos & Barbas, 2013; Stoner *et al*, 2014). Interneuron dysfunction and PV expression reduction have been observed in various mouse models of ASD, and PV expression downregulation in mice is sufficient to cause behavioral abnormalities related to all human ASD core symptoms (Wöhr *et al*, 2015; Canetta *et al*, 2016; Filice *et al*, 2016). Together, our studies suggest that ZIKV infection during pregnancy disrupts interneurons and leads to cortical hyperactivity, which in turn contributes to cognitive behavioral abnormalities.

We found that the vHIP hyperactivity contributes to autistic-like behaviors via modulating mPFC functions in ZIKV-affected offspring mice. Despite documentation of vHIP hyperactivity in other cognitive dysfunctions (Sigurdsson *et al*, 2010; Carreno *et al*, 2016; Padilla-Coreano *et al*, 2016; Phillips *et al*, 2019), our finding represents the first discovery of a hyperactive vHIP-mPFC circuit driving social behaviors in a maternal infection-associated neuropsychiatric disorder. Our optogenetic excitation of vHIP fibers resulted in larger EPSC amplitude in their monosynaptically connected pyramidal neurons in the mPFC of ZIKV-affected offspring brains, suggesting enhanced vHIP-mPFC functional connectivity. To identify the neural substrate of this hyperactive vHIP-mPFC pathway, we examined synaptic and cellular targets of mPFC-projecting vHIP axons. Our trans-synaptic tracing results showed that > 85% of labeled vHIP projections innervated cells are excitatory neurons. There is an increased neuronal activity in the layer 5 neurons of the mPFC of ZIKV affected offspring, which is consistent with vHIP inputs' preferential engagement with layer 5 IL neurons (Liu & Carter, 2018). We also identified PV neurons as the interneuron subtype mostly innervated by vHIP axons (Fig 6H), which is reminiscent of previous vHIP-driven feedforward inhibition in the IL (Marek *et al*, 2018; Phillips *et al*, 2019). In the mPFC of ZIKV-affected offspring brains, we found a decrease in vHIP-innervated PV-positive interneurons. The densities of individual vHIP-derived axonal presynaptic boutons were significantly increased, whereas the sizes of vHIP boutons remained unchanged. These results suggest a redistribution of vHIP inputs to different cell types, an altered wiring pattern, and increased vHIP-mPFC connectivity in ZIKV-affected offspring brains, providing insights into neural substrates underlying this hyperactive vHIP-mPFC circuit. Finally, our chemogenetic studies demonstrated the functional importance of this vHIP-mPFC pathway in driving social memory deficits in ZIKV-affected offspring mice. It has been reported that nucleus accumbens (NAc)-projecting vHIP neurons are both necessary and sufficient for social memory (Okuyama *et al*, 2016). Future studies should determine whether there are anatomically and molecularly distinct populations of vHIP neurons projecting to mPFC and NAc, and if so, what are their respective roles in mediating social memory.

In summary, we established and characterized a new mouse model of neurocognitive dysfunctions in children with maternal ZIKV exposure. We identified novel neural substrates and hyperconnectivity of vHIP to mPFC projections responsible for social deficits in ZIKV-affected offspring mice. These findings have prognostic value and implications for network dysregulation in other neuropsychiatric disorders.

Materials and Methods

Animals

All animal experiments were conducted in accordance with the guidelines of the Institutional Animal Care and Use Committee, University of Southern California. C57BL/6 wild-type mice were ordered from Taconic laboratory. Vglut2-ires-Cre (stock No.: 016963) and Ai14 (stock No.: 007914) mice aged 8–16 weeks were obtained from the Jackson Laboratory. Mice were housed in a regular light cycle (7:00 a.m. to 7:00 p.m.) and provided with food and water *ad libitum*.

ZIKA virus

ZIKV MEX1-44 was isolated in Chiapas, Mexico, in January of 2016 from an infected *Aedes aegypti* mosquito and was passaged by the World Reference Center for Emerging Viruses and Arboviruses (WRCEVA) in Vero cells. We obtained this virus with permission through the University of Texas Medical Branch at Galveston (UTMB). As described in previous studies (Shao *et al*, 2016, 2017; Herrlinger *et al*, 2018), we titrated virus using Vero cells (African green monkey kidney epithelial cells) obtained from American Type Culture Collection (ATCC). ZIKV stocks were generated by infecting Vero cells at a multiplicity of infection (MOI) of 0.01 and harvesting supernatants at 96 h and 120 h post-infection. Viral titers were determined by plaque assays as PFU/ml. High titer viral stocks were stored as single use-aliquots and stored at −80°C.

Maternal ZIKV infection

Timed pregnant female mice were obtained by mating with males, and the presence of seminal plugs was considered as embryonic day (E0.5). At E12.5, pregnant female mice received an intravenous injection of either 1.2×10^6 PFU/ml of ZIKV suspended in 200 µl DPBS or 200 µl DPBS as vehicle. Dams were returned to their home cages and monitored for parturition.

Stereotaxic surgeries

Mice were anesthetized with isoflurane (induction 2.5%, maintenance 1.5%) and aligned in a stereotactic frame (KOPF instruments, Tujunga, CA). The skull was exposed under antiseptic conditions, and a small craniotomy was made with a thin drill. Virus or neural tracer was delivered through a 10 µl syringe (Hamilton Company, Reno, NV) at a rate of 50 nl/min. For anterograde transneuronal labeling, AAV1-hSyn-Cre (Addgene #105553, 1.8×10^{13} GC/ml) was injected into vHIP (300 nl total volume; AP −3.3 mm. ML ± 3.5 mm, DV −3 mm) of Ai14 mice. Mice were euthanized 4 weeks after injection for examination. For axon tracing of vHIP to mPFC projections, AAV9-CAG-eGFP (Upenn Vector Core, 1.1×10^{14} GC/ml) was diluted to 1% with sterile PBS and injected into vHIP (100 nl total volume; AP −3.3 mm. ML ± 3.5 mm, DV −3 mm). Mice were euthanized 4 weeks after injection. 150 µm-thick coronal sections were collected to image vHIP axon terminals in mPFC. To measure the output connectivity of vHIP to mPFC, AAV5-CaMKIIa-hChR2-Cherry (UNC Vector Core, 4.5×10^{12} GC/ml) was injected into vHIP (300 nl total volume; AP −3.3 mm. ML ± 3.5 mm, DV −3 mm). Mice were euthanized 3–4 weeks after injection. 300 µm-thick

coronal sections in mPFC were collected for slice recording. For chemogenetic manipulation with DREADD and CNO, AAVretro-Cre (UNC Vector Core, 2.8×10^{12} GC/ml) was injected into mPFC (300 nL total volume; AP +1.7 mm. ± ML 0.3 mm, DV −1.8 mm). After 2–7 days, a second injection of AAV2-hSyn-DIO-hM4Di-mCherry (Addgene #44363, 1.4×10^{13} GC/ml) or AAV2-hSyn-DIO-mCherry (Addgene #50459, 4.9×10^{12} GC/ml) was injected into vHIP (300 nl total volume; AP −3.3 mm. ML ± 3.5 mm, DV −3 mm).

Serum collection and ELISA

Mice were anesthetized with isoflurane (induction 2.5%, maintenance 1.5%), and blood samples were collected from orbital sinus into the Eppendorf tubes. We allow the blood to clot by leaving it undisturbed at room temperature for 60 min and remove the clot by centrifuging at 2,500 *g* for 15 min at 4°C. The supernatant serum was used for IL-17a ELISA measurement according to the manufacturer's protocol (BioLegend).

Real-time PCR

Total RNA was extracted from the cerebral cortex of E14.5 embryonic brain. 2 μg RNA was reverse transcribed into cDNA using SuperScript III first-strand synthesis for RT–PCR (Invitrogen). The mRNA levels of Il17ra and Gapdh genes were quantified with a Real-Time PCR System. RT–PCR was conducted under the following cycling conditions: 95°C for 10 min for pre-denaturation, followed by 40 cycles of 95°C for 15 s and 60°C for 1 min. The last step was conducted at 95°C for 15 s, 60°C for 15 s, and 95°C for 15 s for a melting curve of the PCR products to confirm the specificity of amplification. The relative mRNA abundances were analyzed utilizing the $2^{-\Delta\Delta Ct}$ method with Gapdh as a reference and plotted as fold changes compared with the mock-treated samples. The detailed nucleotide sequences are shown as follows:

Il17ra 5'-AGATGCCAGCATCCTGTACC-3' and 5'-CACAGTCACA GCGTGTCTCA- 3'; Gapdh 5'- GACTTCAACAGCCTCCCACTCTTCC-3' and 5'-TGGGTGGTCCAGGTTTCTTACTCCTT-3'.

Immunofluorescence

Animals were deeply anesthetized and transcardially perfused with phosphate-buffered saline (PBS) followed by 4% paraformaldehyde. Brains were post-fixed at 4°C overnight in 4% paraformaldehyde, then incubated in 30% sucrose/PBS solution for 2 days and embedded in Tissue-Tek OCT compound (Sakura). Coronal sections were sliced at 40 μm using a cryostat (Leica CM1950). Sections were washed in PBS three times (5 min each time) and then incubated with blocking solution (5% normal goat serum, 1% BSA, 0.3% Triton X-100 in PBS) for 2 h at room temperature. Sections were then incubated with mouse anti-Flavivirus group antigens (1:200, GTX57154, GeneTex), rabbit anti-Iba1 (1:400, 019-19741, Wako), rat anti-CD68 (1:200, MCA1957, Bio-Rad), rabbit anti-c-fos (1:400; 2250, CST), rabbit anti-Parvalbumin (1:400; PV27, Swant), rat anti-Somatostatin (1:200; MAB354, Millipore), mouse anti-Calretinin (1:400; MAB1568, Millipore), guinea pig anti-vGLUT1 (1:200; AB5905, Millipore), and rabbit anti-vGAT (1:200; 131002, Synaptic Systems) in blocking solution overnight at 4°C. After washing in PBS three times (5 min each time), sections were incubated with species-specific fluorescently conjugated secondary antibodies (1:200, Invitrogen) and DAPI (1:1,000) in blocking solution for 2 h at room temperature. After washing in PBS three times for 5 min each time, sections were mounted on glass slides with mounting medium and coverslipped. Images of stained sections were acquired using a confocal microscope with 10×, 20×, or 60× objective lens. All images were taken using identical laser power, gain, and offset values.

Imaging and quantification of presynaptic terminals

Mice were perfused 4 weeks after virus injection, and 150 μm-thick coronal sections were collected to image vHIP axon terminals in the mPFC. All images were acquired with setting as z-series (stacks as 1 μm depth interval) using a 63× (1.4 NA) Leica oil immersion objective with identical parameters (laser power, gain, and offset). Axons were semi-manually traced using NCTracer, and bouton density and size were quantified using Bouton Analyzer running in MATLAB (MathWorks, Natick, MA).

Behavioral testing

Mice were acclimated to the behavioral testing room at least 60 min before the behavioral tests. Three-chamber social interaction test was performed in a Plexiglas box containing three compartments connected by small openings that allowed mice free access to each compartment. Subject mouse was first placed in the middle chamber with side doors open to allow it to freely explore the three empty chambers. After 10 min of habituation, the mouse was gently guided to the middle chamber and side doors were closed. A stranger mouse was placed in the inverted wire cup in one side chamber, and an empty wire cup was placed in the other side chamber. Then, the side doors were opened and the subject mouse was allowed to freely explore the chambers for 10 min. After this period, the subject mouse was again guided into the middle chamber and side doors were closed. A second stranger mouse was placed in the previous empty wire cup. The side doors were opened, and the subject mouse was allowed to freely explore for another 10 min. The amount of time that the subject mouse spent sniffing each wire cup was quantified and the preference index was calculated as $(Ts1 - Te)/Ts1 + Te)*100\%$ and $(Ts2 - Ts1)/Ts2 + Ts1)*100\%$. Here, Te, Ts1, and Ts2 represent the time spent exploring empty, stranger 1, and stranger 2 wire cup, respectively. The apparatus and wire cups were thoroughly cleaned with 75% ethanol to remove the olfactory cues between tests for each mouse. For hM4Di-mediated inhibition experiment, the three-chamber social interaction test was performed 4–6 weeks after virus injection. Mice were given i.p. injections of CNO (3 mg/kg body weight) one hour before the behavioral test. Mice were perfused two hours after behavioral testing and brains were collected for c-fos immunostaining.

The five-trial social interaction test was performed as described previously (Hitti & Siegelbaum, 2014). Briefly, subject mice were singly housed for three days. On the day of testing, the subject mice were placed in the clean cage and presented with a caged stranger mouse for five consecutive 1-minute trials with an inter-trial interval of 1 min. A novel stranger mouse was presented on the sixth trial. The sniffing time was manually recorded. The percent baseline of trials 2–6 was calculated by dividing sniffing time in each trial by that of trial 1.

Novel object test was performed as described previously with minor modifications (Leger *et al*, 2013). Briefly, this test consists of habituation, familiarization, and test phases. In the habituation phase, subject mice were placed in the center of a clean mouse cage and allowed to explore freely for 5 min. After 24 h, the familiarization phase was performed. Two identical objects were taped to floor along the long axis, 10 cm away from the south and north walls. The mouse was placed in the center of the cage facing the east or west wall and allowed to explore for 10 min. The test phase was performed 24 h after the familiarization phase. One of the identical objects was replaced with a novel object with a different shape but similar size. The mouse was placed in the center of the cage facing the east or west wall and allowed to explore for 10 min. The apparatus and objects were thoroughly cleaned with 75% ethanol to remove the olfactory cues between each trial. The entire test phase was videotaped, and the travel of the subject mouse was manually documented. The preference index was calculated as (Tn − Tf)/(Tn + Tf) × 100%, where Tn and Tf represent the time spent exploring novel and familiar objects, respectively.

Self-grooming test was performed in the clean, empty mouse cage. Each mouse was allowed to freely explore the mouse cage for 20 min continuously. The first 10 min period was habituation, and only the second 10 min period was recorded for scoring of cumulative self-grooming time.

Odor discrimination and habituation test was performed as described previously (Yu *et al*, 2021). Each mouse was habituated for one hour to a clean new cage before test. Then, the animal was presented five odors in a row delivered on cotton swabs in the following order: water, almond flavor, banana flavor, social odor 1, and social odor 2. The almond and banana odors were prepared by diluting almond and citrus extracts (McCormick) in distilled water (1:100). Each social odor was prepared by wiping a cotton swab for 15 s in a zigzag fashion across the bottom of dirty cage which was used to keep mice of the same sex as the test subject. Each odor was presented three times in a row for 2 min each time with approximately 1 min inter-trial interval. For every non-social odor exposure, the cotton swab was freshly prepared by applying 50 μl of diluted odorant. The cumulative time spent sniffing the odor (the animal's nose was oriented toward the cotton tip at a distance less than 2 cm) was manually recorded.

Looming spot test was performed in an open-top box with dimension of 40cm x 40cm x 40cm. An opaque shelter was placed in the corner of the chamber with an entrance facing the center of the arena. Each subject mouse was placed in the center of the apparatus with the white monitor screen above and given at least 10 min for acclimation. The visual stimulus was programmed and displayed using the Psychtoolbox module for MATLAB. A spherical, black looming stimulus was initiated on a white background once the subject mouse was away from the shelter. The stimulus expanded from 2 degrees of visual angle to 55 degrees in 200 ms and persisted for 300 ms and then restarted the sequence with a 500ms delay for a total number of 10 repeats. The fear response was considered positive if the subject mouse either froze or fled into the cup within 5 s of the stimulus initiation. The fear response was considered negative if the subject did not demonstrate any flight or freezing behavior.

Forelimb grip strength test: The grip strength meter (Bioseb, BIO-GS3) was used to measure the forelimb grip strength. The gauge was reset and stabilized to 0 g before testing each mouse. A mouse was allowed to grasp the bar mounted on the force gauge and the mouse's tail was slowly pulled back. The peak pull force in grams was recorded on a digital force transducer.

Rotarod test: The rotarod test consists of training and test phases. Mice were first trained by placing them on a rotating rod (Panlab, Harvard Apparatus) at a constant speed of 4 rpm until they were able to stay on the rotating rod for 20 s. The test phase was performed 24 h after the training phase. The rotarod apparatus was set to accelerate from 4 to 40 rpm in 300 s, and subject mice were placed on the rod initially rotating at 4 rpm. The latency (time) to falling off the rod was determined. Each mouse was tested three times a day at 15-min intervals for three consecutive days.

Slice preparation and recording

Mice were deeply anesthetized with Ketamine/Xylazine (100/10 mg/Kg, i.p.) and then decapitated. Coronal slices (thickness, 300 μm) were cut using a vibratome (10111N, Ted Pella) in the ice-cold dissection buffer (composition: 60 mM NaCl, 3 mM KCl, 1.25 mM NaH_2PO_4, 25 mM $NaHCO_3$, 115 mM sucrose, 10 mM glucose, 7 mM $MgCl_2$, 0.5 mM $CaCl_2$; saturated with 5% CO_2 balanced O_2; pH = 7.4). Slices were recovered for 30 min in a submersion chamber filled with 35 °C artificial cerebrospinal fluid (aCSF) (composition:119 mM NaCl, 26.2 mM $NaHCO_3$, 11 mM glucose, 2.5 mM KCl, 2 mM $CaCl_2$, 2 mM $MgCl_2$, and 1.2 mM NaH_2PO_4, 2 mM Sodium Pyruvate, 0.5 mM Vitamin C) and then kept at room temperature for > 40 min until use. Cells were visualized using Olympus BX51 WI equipped with a 60× water immersion lens. Pyramidal neurons from layer V in mPFC were identified by the morphology and intrinsic membrane properties. Patch pipettes were pulled from borosilicate glass (TW150-1, World Precision Instruments), and the tip resistance was between 4-6 MΩ in aCSF. Whole-cell recordings were performed using a patch-clamp amplifier (Multiclamp 700B, Molecular Devices), and data were acquired and analyzed using pClamp 10 software (Molecular Devices) and Igor pro 6 (WaveMetrics), respectively.

Spontaneous excitatory and inhibitory postsynaptic currents were recorded under voltage-clamp mode at a holding voltage of –70 mV at 10 kHz and low-pass filtered at 2 kHz. For sEPSC recording, internal solution contained: 125 mM cesium gluconate, 2 mM KCl, 10 mM HEPES, 10 mM EGTA, 4 mM ATP, 0.3 mM GTP, and 8 mM phosphocreatine; pH = 7.25; 290–300 mOsm. sEPSC was recorded with aCSF containing 50 μM 2-Amino-5-phosphonopentanoic acid (APV) and 10 μM NBQX. For sIPSC recording, internal solution contained: 125 mM cesium chlorine, 2 mM KCl, 10 mM HEPES, 10 mM EGTA, 4 mM ATP, 0.3 mM GTP, and 8 mM phosphocreatine; pH = 7.25; 290–300 mOsm. sIPSC was recorded with aCSF containing 50 μM APV and 20 μM bicuculine.

Intrinsic excitation of Layer V pyramidal neurons was assessed under current-clamp mode by measuring the firing rate in response to a series of depolarizing pulses while perfusing with aCSF containing 50 μM 2-Amino-5-phosphonopentanoic acid (APV), 10 μM NBQX, and 20 μM bicuculine. Potassium-based internal solution (125 mM potassium gluconate, 2 mM KCl, 10 mM HEPES, 10 mM EGTA, 4 mM ATP, 0.3 mM GTP, and 8 mM phosphocreatine; pH = 7.25; 290–300 mOsm) was used for current-clamp recording.

For the evoked EPSC recording by photostimulation of ChR2 in the mPFC, mice injected with AAV5-CaMKIIa-hChR2-Cherry in vHIP

were used for slice recording. Synaptic responses were induced by delivering the light (excitation wavelength: 470 nm, 5 ms pulse, 5 mW power) to the mPFC via a 40× objective lens. Signals were recorded under voltage-clamp mode at a holding voltage of −70 mV. Cesium-based internal solution (described as above) was used for eEPSC recording.

Data availability

This study includes no data deposited in public database.

Expanded View for this article is available online.

Acknowledgments
We thank Chen laboratory colleagues for stimulating discussions. We are grateful for Bridget Samuels's critical reading of the manuscript. Chen laboratory is supported by funds from the Associate Dean of Research Fund from the Center for Craniofacial Molecular Biology, Herman Ostrow School of Dentistry at the University of Southern California, and grants R01NS097231 (J.C.) and R01NS096176 (J.C.) from the National Institutes of Health.

Conflict of interest
The authors declare that they have no conflict of interest that might be perceived as affecting the objectivity of these studies.

Author contributions
Conception and experiments: LM, JW, JG, YW, WZ, YD, JL, YL, and FW Manuscript writing: GF, RC, BY, ZZ, M-LG, W-KK, and YC. Design and interpretation of experiments and manuscript writing: J-FC and LM.

References

Adams Waldorf KM, Nelson BR, Stencel-Baerenwald JE, Studholme C, Kapur RP, Armistead B, Walker CL, Merillat S, Vornhagen J, Tisoncik-Go J *et al* (2018) Congenital Zika virus infection as a silent pathology with loss of neurogenic output in the fetal brain. *Nat Med* 24: 368 – 374

Amodio DM, Frith CD (2006) Meeting of minds: the medial frontal cortex and social cognition. *Nat Rev Neurosci* 7: 268 – 277

Bateup HS, Johnson CA, Denefrio CL, Saulnier JL, Kornacker K, Sabatini BL (2013) Excitatory/inhibitory synaptic imbalance leads to hippocampal hyperexcitability in mouse models of tuberous sclerosis. *Neuron* 78: 510 – 522

Brasil P, Pereira JP, Moreira ME, Ribeiro Nogueira RM, Damasceno L, Wakimoto M, Rabello RS, Valderramos SG, Halai U-A, Salles TS *et al* (2016) Zika virus infection in pregnant women in Rio de Janeiro. *N Engl J Med* 375: 2321 – 2334

Canetta S, Bolkan S, Padilla-Coreano N, Song LJ, Sahn R, Harrison NL, Gordon JA, Brown A, Kellendonk C (2016) Maternal immune activation leads to selective functional deficits in offspring parvalbumin interneurons. *Mol Psychiatry* 21: 956 – 968

Carreno FR, Donegan JJ, Boley AM, Shah A, DeGuzman M, Frazer A, Lodge DJ (2016) Activation of a ventral hippocampus-medial prefrontal cortex pathway is both necessary and sufficient for an antidepressant response to ketamine. *Mol Psychiatry* 21: 1298 – 1308

Choi GB, Yim YS, Wong H, Kim S, Kim H, Kim SV, Hoeffer CA, Littman DR, Huh JR (2016) The maternal interleukin-17a pathway in mice promotes autism-like phenotypes in offspring. *Science* 351: 933 – 939

Cranston JS, Tiene SF, Nielsen-Saines K, Vasconcelos Z, Pone MV, Pone S, Zin A, Salles TS, Pereira JP, Orofino D *et al* (2020) Association between antenatal exposure to Zika virus and anatomical and neurodevelopmental abnormalities in children. *JAMA Netw Open* 3: e209303

Cui J, Shipley FB, Shannon ML, Alturkistani O, Dani N, Webb MD, Sugden AU, Andermann ML, Lehtinen MK (2020) Inflammation of the embryonic choroid plexus barrier following maternal immune activation. *Dev Cell* 55: 617 – 628

Cui L, Zou P, Chen E, Yao H, Zheng H, Wang Q, Zhu J-N, Jiang S, Lu L, Zhang J (2017) Visual and motor deficits in grown-up mice with congenital Zika virus infection. *EBioMedicine* 20: 193 – 201

de la Torre-Ubieta L, Won H, Stein JL, Geschwind DH (2016) Advancing the understanding of autism disease mechanisms through genetics. *Nat Med* 22: 345 – 361.

Dembrow NC, Chitwood RA, Johnston D (2010) Projection-specific neuromodulation of medial prefrontal cortex neurons. *J Neurosci* 30: 16922 – 16937

Einspieler C, Utsch F, Brasil P, Panvequio Aizawa CY, Peyton C, Hydee Hasue R, Françoso Genovesi F, Damasceno L, Moreira ME, Adachi K *et al* (2019) Association of infants exposed to prenatal zika virus infection with their clinical, neurologic, and developmental status evaluated via the general movement assessment tool. *JAMA Netw Open* 2: e187235

Estes ML, McAllister AK (2016) Maternal immune activation: Implications for neuropsychiatric disorders. *Science* 353: 772 – 777

Euston DR, Gruber AJ, McNaughton BL (2012) The role of medial prefrontal cortex in memory and decision making. *Neuron* 76: 1057 – 1070

Filice F, Vörckel KJ, Sungur AÖ, Wöhr M, Schwaller B (2016) Reduction in parvalbumin expression not loss of the parvalbumin-expressing GABA interneuron subpopulation in genetic parvalbumin and shank mouse models of autism. *Mol Brain* 9: 10 – 17

Forbes CE, Grafman J (2010) The role of the human prefrontal cortex in social cognition and moral judgment. *Annu Rev Neurosci* 33: 299 – 324

Gabbott P, Headlam A, Busby S (2002) Morphological evidence that CA1 hippocampal afferents monosynaptically innervate PV-containing neurons and NADPH-diaphorase reactive cells in the medial prefrontal cortex (Areas 25/32) of the rat. *Brain Res* 946: 314 – 322

Geschwind DH, Levitt P (2007) Autism spectrum disorders: developmental disconnection syndromes. *Curr Opin Neurobiol* 17: 103 – 111

Golden CE, Buxbaum JD, De Rubeis S (2018) Disrupted circuits in mouse models of autism spectrum disorder and intellectual disability. *Curr Opin Neurobiol* 48: 106 – 112

Herrlinger SA, Shao Q, Ma L, Brindley M, Chen J-F (2018) Establishing mouse models for zika virus-induced neurological disorders using intracerebral injection strategies: embryonic, neonatal, and adult. *J Vis Exp* 134: e56486

Hitti FL, Siegelbaum SA (2014) The hippocampal CA2 region is essential for social memory. *Nature* 508: 88 – 92

Hoen B, Schaub B, Funk AL, Ardillon V, Boullard M, Cabié A, Callier C, Carles G, Cassadou S, Césaire R *et al* (2018) Pregnancy outcomes after ZIKV infection in French territories in the Americas. *N Engl J Med* 378: 985 – 994

Honein MA, Dawson AL, Petersen EE, Jones AM, Lee EH, Yazdy MM, Ahmad N, Macdonald J, Evert N, Bingham A *et al* (2017) Birth defects among fetuses and infants of US women with evidence of possible Zika virus infection during pregnancy. *JAMA* 317: 59 – 68

Kepecs A, Fishell G (2014) Interneuron cell types are fit to function. *Nature* 505: 318 – 326

Knuesel I, Chicha L, Britschgi M, Schobel SA, Bodmer M, Hellings JA, Toovey S, Prinssen EP (2014) Maternal immune activation and abnormal brain development across CNS disorders. *Nat Rev Neurol* 10: 643 – 660

Kohil A, Jemmieh S, Smatti MK, Yassine HM (2021) Viral meningitis: an overview. *Arch Virol* 166: 335 – 345

Leger M, Quiedeville A, Bouet V, Haelewyn B, Boulouard M, Schumann-Bard P, Freret T (2013) Object recognition test in mice. *Nat Protoc* 8: 2531 – 2537

Li C, Xu D, Ye Q, Hong S, Jiang Y, Liu X, Zhang N, Shi L, Qin C-F, Xu Z (2016) Zika Virus disrupts neural progenitor development and leads to microcephaly in mice. *Cell Stem Cell* 19: 120 – 126

Liu X, Carter AG (2018) Ventral hippocampal inputs preferentially drive corticocortical neurons in the infralimbic prefrontal cortex. *J Neurosci* 38: 7351 – 7363

Marek R, Jin J, Goode TD, Giustino TF, Wang Q, Acca GM, Holehonnur R, Ploski JE, Fitzgerald PJ, Lynagh T *et al* (2018) Hippocampus-driven feed-forward inhibition of the prefrontal cortex mediates relapse of extinguished fear. *Nat Neurosci* 21: 384 – 392

Martinot AJ, Abbink P, Afacan O, Prohl AK, Bronson R, Hecht JL, Borducchi EN, Larocca RA, Peterson RL, Rinaldi W *et al* (2018) Fetal neuropathology in Zika virus-infected pregnant female rhesus monkeys. *Cell* 173: 1111 – 1122

Miner JJ, Cao B, Govero J, Smith AM, Fernandez E, Cabrera OH, Garber C, Noll M, Klein RS, Noguchi KK *et al* (2016) Zika virus infection during pregnancy in mice causes placental damage and fetal demise. *Cell* 165: 1081 – 1091

Ming G-L, Tang H, Song H (2016) Advances in Zika virus research: stem cell models, challenges, and opportunities. *Cell Stem Cell* 19: 690 – 702

Mulkey SB, Arroyave-Wessel M, Peyton C, Bulas DI, Fourzali Y, Jiang J, Russo S, McCarter R, Msall ME, du Plessis AJ *et al* (2020) Neurodevelopmental abnormalities in children with in utero Zika virus exposure without congenital Zika syndrome. *JAMA Pediatr* 174: 269 – 276

Nielsen-Saines K, Brasil P, Kerin T, Vasconcelos Z, Gabaglia CR, Damasceno L, Pone M, Abreu de Carvalho LM, Pone SM, Zin AA *et al* (2019) Delayed childhood neurodevelopment and neurosensory alterations in the second year of life in a prospective cohort of ZIKV-exposed children. *Nat Med* 375: 2321 – 2325

Okuyama T, Kitamura T, Roy DS, Itohara S, Tonegawa S (2016) Ventral CA1 neurons store social memory. *Science* 353: 1536 – 1541

Ornelas AMM, Pezzuto P, Silveira PP, Melo FO, Ferreira TA, Oliveira-Szejnfeld PS, Leal JI, Amorim MMR, Hamilton S, Rawlinson WD *et al* (2017) Immune activation in amniotic fluid from Zika virus-associated microcephaly. *Ann Neurol* 81: 152 – 156

Padilla-Coreano N, Bolkan SS, Pierce GM, Blackman DR, Hardin WD, Garcia-Garcia AL, Spellman TJ, Gordon JA (2016) Direct ventral hippocampal-prefrontal input is required for anxiety-related neural activity and behavior. *Neuron* 89: 857 – 866

Paul AM, Acharya D, Neupane B, Thompson EA, Gonzalez-Fernandez G, Copeland KM, Garrett M, Liu H, Lopez ME, de Cruz M *et al* (2018) Congenital Zika virus infection in immunocompetent mice causes postnatal growth impediment and neurobehavioral deficits. *Front Microbiol* 9: 2028

Peçanha PM, Gomes Junior SC, Pone SM, Pone MVDS, Vasconcelos Z, Zin A, Vilibor RHH, Costa RP, Meio MDBB, Nielsen-Saines K *et al* (2020) Neurodevelopment of children exposed intra-uterus by Zika virus: A case series. *PLoS One* 15: e0229434

Pessoa A, van der Linden V, Yeargin-Allsopp M, Carvalho MDCG, Ribeiro EM, Van Naarden Braun K, Durkin MS, Pastula DM, Moore JT, Moore CA (2018) Motor abnormalities and epilepsy in infants and children with evidence of congenital Zika virus infection. *Pediatrics* 141: S167 – S179

Phillips ML, Robinson HA, Pozzo-Miller L (2019) Ventral hippocampal projections to the medial prefrontal cortex regulate social memory. *Elife* 8: 679

Rothwell PE, Fuccillo MV, Maxeiner S, Hayton SJ, Gokce O, Lim BK, Fowler SC, Malenka RC, Südhof TC (2014) Autism-associated neuroligin-3 mutations commonly impair striatal circuits to boost repetitive behaviors. *Cell* 158: 198 – 212

Rustenhoven J, Drieu A, Mamuladze T, de Lima KA, Dykstra T, Wall M, Papadopoulos Z, Kanamori M, Salvador AF, Baker W *et al* (2021) Functional characterization of the dural sinuses as a neuroimmune interface. *Cell* 184: 1000 – 1016

Sahin M, Sur M (2015) Genes, circuits, and precision therapies for autism and related neurodevelopmental disorders. *Science* 350: aab3897

Selimbeyoglu A, Kim CK, Inoue M, Lee SY, Hong ASO, Kauvar I, Ramakrishnan C, Fenno LE, Davidson TJ, Wright M *et al* (2017) Modulation of prefrontal cortex excitation/inhibition balance rescues social behavior in CNTNAP2-deficient mice. *Sci Transl Med* 9: eaah6733

Shao Q, Herrlinger S, Yang S-L, Lai F, Moore JM, Brindley MA, Chen J-F (2016) Zika virus infection disrupts neurovascular development and results in postnatal microcephaly with brain damage. *Development* 143: 4127 – 4136

Shao Q, Herrlinger S, Zhu Y-N, Yang M, Goodfellow F, Stice SL, Qi X-P, Brindley MA, Chen J-F (2017) The African Zika virus MR-766 is more virulent and causes more severe brain damage than current Asian lineage and dengue virus. *Development* 144: 4114 – 4124

Shapiro-Mendoza CK, Rice ME, Galang RR, Fulton AC, VanMaldeghem K, Prado MV, Ellis E, Anesi MS, Simeone RM, Petersen EE *et al* (2017) Pregnancy outcomes after maternal Zika virus infection during pregnancy – U.S. Territories, January 1, 2016-April 25, 2017. *MMWR Morb Mortal Wkly Rep* 66: 615 – 621

Shi Y, Li S, Wu Q, Sun L, Zhang J, Pan N, Wang Q, Bi Y, An J, Lu X *et al* (2018) Vertical transmission of the Zika virus causes neurological disorders in mouse offspring. *Sci Rep* 8: 3541

Shin Yim Y, Park A, Berrios J, Lafourcade M, Pascual LM, Soares N, Yeon Kim J, Kim S, Kim H, Waisman A *et al* (2017) Reversing behavioural abnormalities in mice exposed to maternal inflammation. *Nature* 549: 482 – 487

Sigurdsson T, Stark KL, Karayiorgou M, Gogos JA, Gordon JA (2010) Impaired hippocampal-prefrontal synchrony in a genetic mouse model of schizophrenia. *Nature* 464: 763 – 767

Silverman JL, Yang M, Lord C, Crawley JN (2010) Behavioural phenotyping assays for mouse models of autism. *Nat Rev Neurosci* 11: 490 – 502

Sohal VS, Rubenstein JLR (2019) Excitation-inhibition balance as a framework for investigating mechanisms in neuropsychiatric disorders. *Mol Psychiatry* 24: 1248 – 1257

Soriano-Arandes A, Frick MA, García López-Hortelano M, Sulleiro E, Rodó C, Sánchez-Seco MP, Cabrera-Lafuente M, Suy A, De la Calle M, Santos M *et al* (2020) Clinical outcomes of a Zika virus mother-child pair cohort in Spain. *Pathogens* 9: 352

Stanelle-Bertram S, Walendy-Gnirß K, Speiseder T, Thiele S, Asante IA, Dreier C, Kouassi NM, Preuß A, Pilnitz-Stolze G, Müller U *et al* (2018) Male offspring born to mildly ZIKV-infected mice are at risk of developing neurocognitive disorders in adulthood. *Nat Microbiol* 3: 1161 – 1174

Sternson SM, Roth BL (2014) Chemogenetic tools to interrogate brain functions. *Annu Rev Neurosci* 37: 387 – 407

Stoner R, Chow ML, Boyle MP, Sunkin SM, Mouton PR, Roy S, Wynshaw-Boris A, Colamarino SA, Lein ES, Courchesne E (2014) Patches of disorganization in the neocortex of children with autism. *N Engl J Med* 370: 1209 – 1219

Thierry AM, Gioanni Y, Dégénétais E, Glowinski J (2000) Hippocampo-prefrontal cortex pathway: anatomical and electrophysiological characteristics. *Hippocampus* 10: 411 – 419

Wheeler AC, Toth D, Ridenour T, Lima Nóbrega L, Borba Firmino R, Marques da Silva C, Carvalho P, Marques D, Okoniewski K, Ventura LO *et al* (2020) Developmental outcomes among young children with congenital Zika syndrome in Brazil. *JAMA Netw Open* 3: e204096

Wöhr M, Orduz D, Gregory P, Moreno H, Khan U, Vörckel KJ, Wolfer DP, Welzl H, Gall D, Schiffmann SN *et al* (2015) Lack of parvalbumin in mice leads to behavioral deficits relevant to all human autism core symptoms and related neural morphofunctional abnormalities. *Transl Psychiatry* 5: e525

Yizhar O, Fenno LE, Prigge M, Schneider F, Davidson TJ, O'Shea DJ, Sohal VS, Goshen I, Finkelstein J, Paz JT *et al* (2011) Neocortical excitation/inhibition balance in information processing and social dysfunction. *Nature* 477: 171 – 178

Yu M, Ma L, Yuan Y, Ye X, Montagne A, He J, Ho T-V, Wu Y, Zhao Z, Sta Maria N *et al* (2021) Cranial suture regeneration mitigates skull and neurocognitive defects in Craniosynostosis. *Cell* 184: 243 – 256

Zikopoulos B, Barbas H (2013) Altered neural connectivity in excitatory and inhibitory cortical circuits in autism. *Front Hum Neurosci* 7: 609